Article

{HPO$_3$} and {WO$_4$} Simultaneously Induce the Assembly of Tri-Ln(III)-Incorporated Antimonotungstates and Their Photoluminescence Behaviors

Xin Xu, Xiaoyi Liu, Dan Wang, Xuejun Liu, Lijuan Chen,* and Junwei Zhao*

Read Online

ACCESS | Metrics & More | Article Recommendations | Supporting Information

ABSTRACT: A double template agent strategy has been adopted to prepare a group of triacetate-adorned tri-Ln(III)-incorporated trimeric antimonotungstates (AMTs) K$_3$Na$_{21}$H[Ln$_3$(CH$_3$COO)$_3$(HPO$_3$)(WO$_4$)][B-α-SbW$_9$O$_{33}$]$_3$·36H$_2$O [Ln = Eu^{3+} (**1**), Dy^{3+} (**2**), Ho^{3+} (**3**), or Er^{3+} (**4**)] in a CH$_3$COOH−CH$_3$COONa buffer system. Therein, H$_3$PO$_3$ and Na$_2$WO$_4$·2H$_2$O have been, respectively, transformed into the capped {HPO$_3$} and {WO$_4$} tetrahedra during the assembly process, which are situated at the center of polyoxoanions of **1−4** and simultaneously perform as structure-directing templates to induce the assembly of **1−4**. The hexahedral configuration supramolecular stacking is the same as the shape of a crystal of **1**, which illustrates that the supramolecular stacking mode plays a significant role in forming the crystal shape of **1−4**. Under the Ln^{3+} f−f excitation, the photoluminescence behaviors involving the emission spectrograms and fluorescence decay curves of **1−4** were systematically researched. The modulation of the excitation wavelength has realized the emission color tuning from blue to red, blue to green, blue to yellow, and green to yellow for **1−4**. On the basis of the excitation of O → W charge transfer (OWCT), the energy-transfer procedure from AMT units to Eu^{3+} centers in **1** is mainly accomplished in the form of energy reabsorption. This work proposes a typical case for the construction of a new type of AMT clusters by using the double template agent strategy and confirms the great potential of Ln-containing AMTs in optic applications.
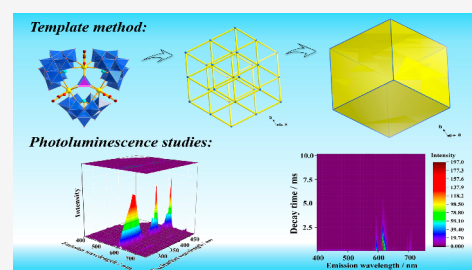
INTRODUCTION

Polyoxometalates (POMs) are a remarkable group of prominent structure-featuring polymetallic oxides that are applicable in many fields, such as luminescence, catalysis, electrochemical sensing, energy, bioactivity, and so forth.[1−7] A significant feature of POM chemistry is that POM building blocks can usually be flexibly assembled through various connection or bonding modes, which will lead to a wide diversity of POM-based materials with varietal structures, sizes, and shapes.[8−10] In a polyoxotungstate (POT) system, the heteroatom-incorporated POT materials have evoked immense attention because extra heteroatoms can tune the structural configuration and stabilize the architecture frameworks of POT subunits.[11,12] Owing to the template effect of heteroatoms, plenary Keggin-type POT moieties can release three {WO$_6$} octahedra and convert them into representative trivacant POT subunits including Keggin-type [XW$_9$O$_{33}$]$^{n−}$ (X = Te^{IV}, Se^{IV}, n = 8; Sb^{III}, As^{III}, Bi^{III}, n = 9) and [XW$_9$O$_{34}$]$^{n−}$ (X = As^V, P^V, n = 9; Ge^{IV}, Si^{IV}, n = 10) subunits with and without the lone-pair electrons.[13] Trilacunary POT subunits feature high-surface-negative charges and intense nucleophilicity toward second metal centers such as transition-metal (TM) centers and lanthanide (Ln) centers; then, they generally serve as superior inorganic multidentate ligands to fabricate TM- or Ln-containing poly(POT) clusters containing a large variety of nuclearities.[14−16] Moreover, trivalent Ln^{3+} centers possess a flexible coordination mode, a high coordination number, and evident coordination selectivity for O atoms, which can easily tune the combination between trilacunary POT subunits and carboxylic ligands.[17−19] Therefore, the above-mentioned assembly rules provide excellent preconditions for the construction of organic-ligand-adorned Ln-incorporated POTs (OLALnPOTs).

Over the past decades, the antimonotungstate (AMT) family based on trivacant Keggin [B-α-SbW$_9$O$_{33}$]$^{9−}$ moieties has developed as an important subfamily of POMs, yet only a few organic-ligand-adorned Ln-incorporated AMTs (OLAL-nAMTs) have been addressed.[20] In 2015, Li et al. prepared two types of picolinate-adorned Ln-incorporated AMTs, [Ln$_2$(H$_2$O)$_4${WO$_2$(pic)}$_2$(B-α-SbW$_8$O$_{30}$)$_2$]$^{10−}$ (Ln = La^{3+}, Pr^{3+}) and [{Ln(H$_2$O)} {Ln(pic)}(Sb$_3$O$_4$)(B-α-SbW$_8$O$_{31}$)(B-α-SbW$_{10}$O$_{35}$)]$_2^{24−}$ (Ln = Tb^{3+}, Dy^{3+}, Ho^{3+}),[21] and Zhao's group acquired two types of Fe−Ln heterometallic sandwich-type AMTs, [Pr(H$_2$O)$_8$][Pr(H$_2$O)$_6$][Fe$_4$(H$_2$O)$_{10}$(B-β-Sb W$_9$O$_{33}$)$_2$]·16H$_2$O and [Ln(H$_2$O)$_7$]$_2$[Fe$_4$(H$_2$O)$_{10}$(B-β-
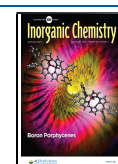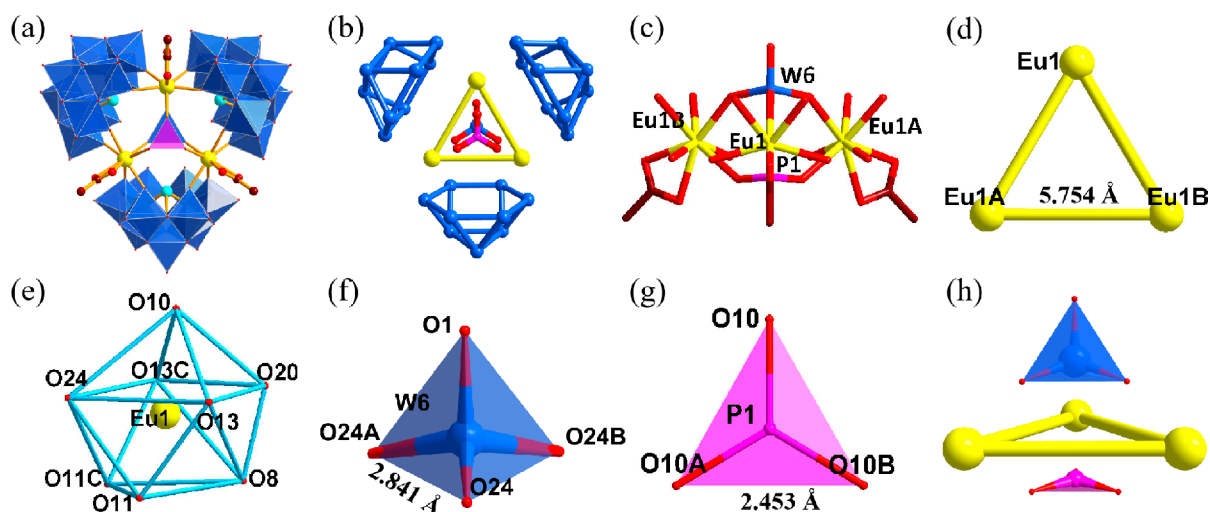
Figure 1. (a) Structure of **A**. (b) Simplified structure of **A**. (c) Structure of **B**. (d) Triangle geometry formed by Eu1^{3+}, EuA^{3+}, and Eu1B^{3+} ions. (e) Coordinated sphere of the Eu1^{3+} ion. (f) Capped {WO$_4$} tetrahedron. (g) Capped {HPO$_3$} tetrahedron. (h) Simplified diagram of **B**. Code: {WO$_4$}, navy tetrahedron; {WO$_6$}, navy octahedra; P, burgundy balls; W, navy balls; O, red balls; Eu, bright-yellow balls; C, brown balls; Sb, blue balls. Symmetry-operation codes: A: $-1 - x + y$, $2 - x$, z; B: $2 - y$, $3 + x - y$, z; C: x, $3 + x - y$, z.

SbW$_9$O$_{33}$)$_2$]·22 H$_2$O (Ln = Tb^{3+}, Dy^{3+}, Lu^{3+}).[22] In 2016, Reinoso and coworkers obtained a series of TM−Ln-substituted heterometal AMTs, [Sb$_7$W$_{36}$O$_{133}$ Ln$_3$TM$_2$(OAc)-(H$_2$O)$_8$]$^{17-}$ (Ln = La^{3+}−Gd^{3+}, TM = Co^{2+}; Ln = Ce^{3+}, TM = Ni^{2+}, Zn^{2+}).[23] Subsequently, Zhao's group synthesized 2-picolinate-adorned Fe−Ln-substituted AMTs, [Ln-(H$_2$O)$_5$]$_2$[Fe$_4$(H$_2$O)$_2$(pic)$_4$(B-β-SbW$_9$O$_{33}$)$_2$]$^{4-}$ and {[Ln-(H$_2$O)$_6$]$_2$ [Fe$_4$(H$_2$O)$_2$(Hpic)$_2$(pic)$_2$(B-β-SbW$_9$O$_{33}$)$_2$]}$^{24-}$ (Ln = Gd^{3+}, Dy^{3+}),[24] and a group of Sb−Ln cluster-connecting AMTs, {[Ln$_4$(H$_2$O)$_6$ Sb$_6$O$_4$] (B-α-SbW$_{10}$O$_{37}$)$_2$(B-α-SbW$_8$O$_{31}$)$_2$}$^{22-}$ (Ln = Dy^{3+}, Ho^{3+}, Er^{3+}).[25]

Up to now, a few well-known structure assembly strategies such as the template method, building block strategy, and time-dependent concept have been reported.[26−29] Some micro-molecular template agents with unique geometries have afforded some POM aggregates with diverse interesting configurations and symmetries, which also cover the range from isolated structures to three-dimensional extended frameworks.[30−33] For instance, Cadot and partners created a series of thiooxomolybdates by using a squarate dication as a template to direct the ring arrangement of [Mo$_2$S$_2$O$_2$(H$_2$O)$_6$]$^{2+}$ units.[34] Kortz and colleagues found that the additional Na$_2$WO$_4$·2H$_2$O can transform into a tetrahedral {WO$_4$} template group to induce the generation of a tri-Y(III)-containing trimeric AMT.[35] Long et al. reported that the CO$_3^{2-}$ anionic template agent can significantly control the formation of trimeric polyoxoanions (POAs).[36] Niu's team adopted the {TeO$_3$} group as a template and connector to construct two phenol-decorated polyoxoniobates.[37] However, few examples of double template agents inducing the aggregation of POM clusters have been reported. Thus we have considered whether two template agents can be used based on the template strategy to construct novel and peculiar architectures, which would also be a great blueprint for the structural design of POMs.

In this work, we have successfully prepared a class of triacetate-adorned tri-Ln(III)-incorporated trimeric AMTs, K$_3$Na$_{21}$H [Ln$_3$(CH$_3$COO)$_3$(HPO$_3$)(WO$_4$)][B-α-SbW$_9$O$_{33}$]$_3$·36H$_2$O [Ln = Eu^{3+}, Dy^{3+}, Ho^{3+}, Er^{3+} (**1−4**)], by using phosphorous acid, sodium tungstate, Na$_9$[B-α-SbW$_9$O$_{33}$]·

19.5H$_2$O, and lanthanide nitrate as reaction materials in a CH$_3$COOH−CH$_3$COONa buffer system (Figure S1). There-in, phosphorous acid and sodium tungstate have been, respectively, transformed into the capped {HPO$_3$} and {WO$_4$} tetrahedra during the assembly process, which are located at the center of POAs and simultaneously perform as structure-directing templates to induce the structures of **1−4**. In the aspect of luminescence behaviors, the characteristic emission and excitation peaks and decay lifetimes of **1−4** were researched systematically at room temperature. Upon the O → W charge transfer (OWCT) excitation, AMT subunits in **1** can transmit energy to Eu^{3+} centers, and the energy-transfer (ET) procedure was mainly completed in the mode of energy reabsorption. This work displays the feasibility of an effective double-template-agent strategy for the fabrication of novel AMT clusters and reveals the great potential of Ln-containing AMT materials in optic applications.

■ RESULTS AND DISCUSSION

Structure. As seen from the crystallographic data in Table S1, **1−4** crystallize in the trigonal space group $R3m$. The oxidation states of W, Sb, and Ln atoms in the POAs of **1−4** are +6, +3, and +3, respectively (Table S2). The good phase purity of these samples is also determined because the powder X-ray diffraction (PXRD) patterns of **1−4** are in good agreement with their single-crystal XRD patterns (Figure S2). Therefore, only the structure description of **1** is exemplified. The molecular unit of **1** is made up of 1 trimeric {[Eu$_3$(CH$_3$COO)$_3$(HPO$_3$)(WO$_4$)][B-α-SbW$_9$O$_{33}$]$_3$}$^{25-}$ (**A**) POA, 3 K$^+$ ions, 21 Na$^+$ ions, 2 protons, and 36 lattice water molecules. The structure of **A** is shown in Figure 1a,b, in which 3 trilacunary [B-α-SbW$_9$O$_{33}$]$^{11-}$ subunits embrace 1 tri-Eu^{3+}-incorporated [Eu$_3$(CH$_3$COO)$_3$(HPO$_3$)(WO$_4$)]$^{2+}$ (**B**) cluster through 12 μ_2-O atoms. Three Sb^{3+} central heteroatoms in three [B-α-SbW$_9$O$_{33}$]$^{11-}$ segments occupy three vertices of an equilateral triangular geometry, and its side length is 7.624 Å (Figure S3a). **B** comprises three [Eu(H$_2$O)]$^{3+}$ ions, three acetate ligands, and two capped {HPO$_3$} and {WO$_4$} tetrahedral groups (Figure 1c). Moreover, three identical crystallographically independent Eu^{3+} centers such as Eu1,
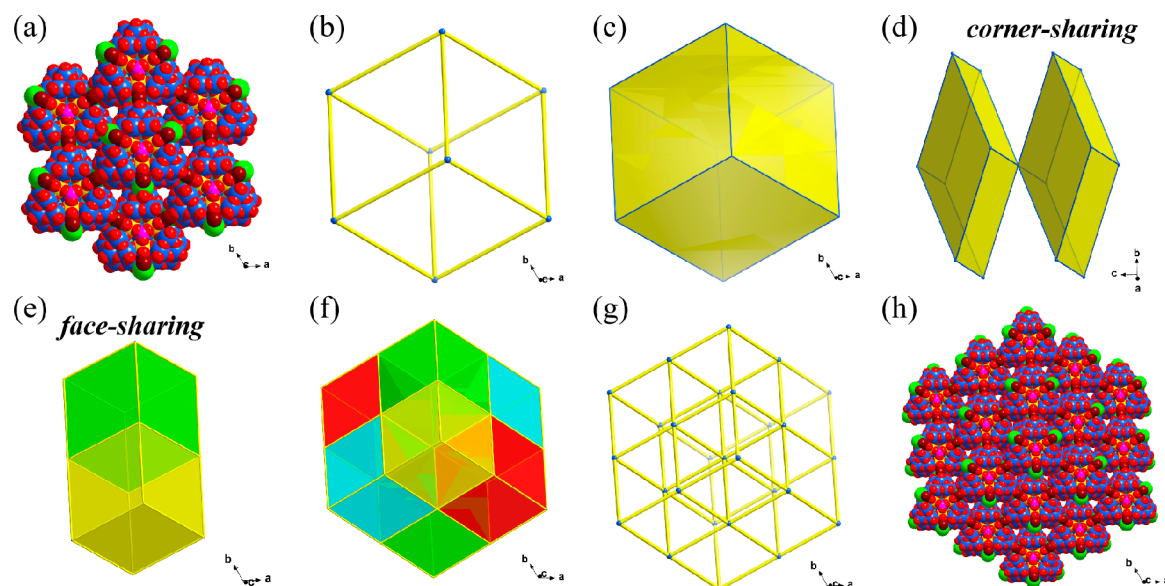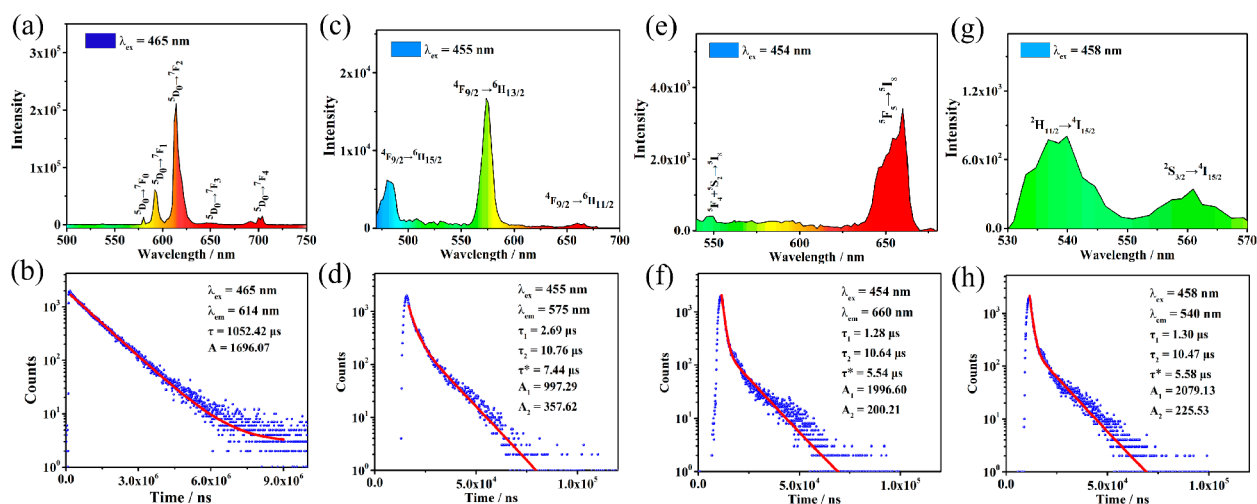
Figure 2. (a) Space-filling structure of the hexagonal alignment of **1**. (b) Topological structure of a hexahedron constituted by eight **A** POAs. (c) Polyhedral representation of a hexahedron constituted by eight **A** POAs. (d) Combination of two corner-sharing hexahedra. (e) Combination of two face-sharing hexahedra. (f) View of a large hexahedron constituted by eight small hexahedra. (g) Topological structure of a large hexahedron comprising 27 **A** POAs. (h) Space-filling view of a large hexahedron comprising 27 **A** POAs.

Figure 3. (a,b) Emission spectrogram and lifetime profile for **1** (λ_{ex} = 465 nm). (c,d) Emission spectrogram and lifetime profile for **2** (λ_{ex} = 455 nm). (e,f) Emission spectrogram and lifetime profile for **3** (λ_{ex} = 454 nm). (g,h) Emission spectrogram and lifetime profile for **4** (λ_{ex} = 458 nm).

Eu1A, and Eu1B also constitute an equilateral triangular geometry (Eu···Eu: 5.754 Å) (Figure 1d). The coordination geometry of these Eu1^{3+} centers belongs to the octa-coordinate distorted monocapped square antiprism, which is determined through four μ_2-O atoms of two neighboring [B-α-SbW$_9$O$_{33}$]$^{11-}$ segments (Eu1–O13: 2.380(10) Å, Eu1–O11: 2.438(12) Å, Eu1–O13C: 2.380(10) Å, Eu1–O11C: 2.438(12) Å), two O atoms (Eu1–O20: 2.495(17) Å, Eu1–O8: 2.452(16) Å) from acetate ligands, one μ_2-O atom of the capped {WO$_4$} tetrahedron (Eu1–O24: 2.37(2) Å), and one μ_2-O atom of the capped {HPO$_3$} tetrahedron (Eu1–O10: 2.41(2) Å) (Figure 1e). Notably, the coordination sphere of Eu1^{3+} comprises no H$_2$O ligand, which was rarely reported in the previous literature. The simplified diagram of **B** exhibits a pyramidal shape in which the capped {WO$_4$} tetrahedron is situated at the top of **B** (Figure S3b). The capped {WO$_4$} tetrahedron is established by three bridging O atoms (e.g.,

O24, O24A, O24B) and one terminal O1 atom. Furthermore, 3 O24 atoms also form an equilateral triangle geometry with a side length of 2.841 Å (Figure 1f). The P^{III}1 atom is located at the center of the {HPO$_3$} tetrahedron, and the H atom sits on one vertex and three O atoms (O10, O10A, and O10B) take up the other three vertices of the {HPO$_3$} tetrahedron. The side length of the equilateral triangle defined by O10, O10A, and O10B atoms is 2.453 Å (Figure 1g). On the basis of the structure-directing template effect of the capped {WO$_4$} and {HPO$_3$} tetrahedrons, three Eu1^{3+} ions form an equilateral triangle arrangement (Figure 1h), and three [B-α-SbW$_9$O$_{33}$]$^{11-}$ subunits are also arranged in an equilateral triangular configuration. Therefore, the appearance of the capped {WO$_4$} and {HPO$_3$} tetrahedrons illustrates that the double-template-agent strategy is feasible and effective and exhibits a large development prospect. Each terminal acetate group decorates a Eu^{3+} center by the bridging of O20 and O8 atoms

(Figure S3c), which effectively improves the space utilization of the lattice.

It should be mentioned that three K^+ cations are embedded into the POA cluster and also arranged in an equilateral triangular mode ($K \cdots K$: 6.300 Å) (Figure S3d). If Na^+ cations are not omitted, then they can perform as metal linkers to connect neighboring POAs to each other. The 3-D supramolecular stacked diagram of **1** presents one hexagonal stacked pattern along the *c* axis (Figure 2a). When simplifying POAs as nodes and Na^+ ions as bonds, respectively, the 3-D topology framework of **1** demonstrates that eight POAs can constitute a unique small hexahedron along the *c* axis (Figure 2b,c). There are two connected modes between two neighboring hexahedra, predominantly including corner-sharing and face-sharing fashions (Figure 2d,e). By further expanding the connection of these neighboring hexahedra, it can be found that the eight small hexahedra form a large hexahedron through two main connection fashions (Figure 2f,g). The large hexahedron comprises 27 POAs (Figure 2g,h). It is notable that the hexahedral configuration supramolecular stacking is the same as the shape of the crystal of **1** (Figure S4a–c), which illustrates that the supramolecular stacking mode plays a significant role in forming the crystal shape of **1–4**.

Luminescence Studies. Trivalent Ln^{3+} ions exhibit remarkable optic performances in the ultraviolet (UV) and near-infrared (NIR) regions, such as sharp emission, a long decay lifetime, and a large Stokes shift, which make Ln-incorporated materials attract extensive research enthusiasm.[38,39] The suitable embedment of Ln^{3+} ions into POT clusters allows broad potential optic applications of Ln-incorporated POTs involving photodynamic, white-light-emitting diodes, phototherapy, optical sensor, imaging, and optical communication.[40,41] Herein, the emission spectrogram, excitation spectrogram, lifetime profiles, emission–excitation maps (EEMs), CIE 1931 diagram, and time-resolved emission spectra (TRES) were utilized to investigate the photoluminescence (PL) performances, emission color-tunable properties, and ET process from AMT moieties to Ln^{3+} centers in **1–4**.

Figure 3 contains the emission spectra and decay curves of **1–4**. The emission peaks of **1**, which are recorded at 500–750 nm upon the visible-light excitation at 465 nm, are, respectively, located at 581, 594, 614, 653, and 706 nm, ascribed to the $^5D_0 \rightarrow {}^7F_K$ (K = 0–4) transitions (Figure 3a). According to previous records, the electronic-dipole (ED) $^5D_0 \rightarrow {}^7F_2$ transition of Eu^{3+} centers without centrosymmetry is greatly affected by the coordination environment, but the magnetic-dipole (MD) $^5D_0 \rightarrow {}^7F_1$ transition with centrosymmetry is not sensitive. If Eu^{3+} ions inhabit a low-symmetry microenvironment, then the emission peak at 614 nm (ED $^5D_0 \rightarrow {}^7F_2$ transition) is dominant, and its intensity will be much higher than the emission peak at 594 nm (MD $^5D_0 \rightarrow {}^7F_1$ transition). Through intensity analysis, the specific value of the $^5D_0 \rightarrow {}^7F_2$ and $^5D_0 \rightarrow {}^7F_1$ emissions is calculated as 3.45, indicating that these Eu^{3+} centers in POAs are situated in a low-symmetry microenvironment. When the highest 614 nm emission band is monitored, the excitation spectrum (250–480 nm) of **1** exhibits a series of excitation peaks, where the wide excitation peak (ca. 290–310 nm) stems from the O → W charge transition (the $^1A_{1g} \rightarrow {}^1T_{1u}$ transition) of AMT moieties, and five excitation peaks at 362, 381, 395, 417, and 465 nm arise from the $Eu^{3+} {}^7F_0 \rightarrow {}^5D_4, {}^5L_7, {}^5L_6, {}^5D_3,$ and $^5D_2$ transitions (Figure S6a).[42–57] By measurement and fitting, the

curves of the decay lifetime (λ_{em} = 614 nm) for **1** confirm the one-order exponential function, eq 1

$$[I = I_0 \exp(-t/\tau)] \tag{1}$$

which provides τ of 1052.42 μs (Figure 3b, Table S3).[48] On the basis of the excitation at 455 nm, three predominant f–f emission lines are presented at 486, 575, and 661 nm, respectively, originating from the $^4F_{9/2} \rightarrow {}^6H_J$ (J = 15/2, 13/2, 11/2) transitions of Dy^{3+} cations in the 470–700 nm emission spectrum of **2** (Figure 3c). It is worth mentioning that the $^4F_{9/2} \rightarrow {}^6H_{15/2}$ transition is a MD transition, and its intensity is not sensitive to the variation of coordination environment and crystal field; however, the hypersensitive ED $^4F_{9/2} \rightarrow {}^6H_{13/2}$ transition is susceptible to the local circumstances of Dy^{3+} centers. The intensity ratio of emissions at 486 ($^4F_{9/2} \rightarrow {}^6H_{13/2}$) and 575 ($^4F_{9/2} \rightarrow {}^6H_{15/2}$) nm for **2** has been calculated as 2.12, revealing that the Dy^{3+} centers in POAs of **2** take up the low-symmetry sites. When the 575 nm strongest emission peak is monitored, the excitation spectrum of **2** (240–480 nm) exhibits an OWCT of AMT moieties at 258 nm along with a group of excitation bands at 351, 367, 389, 428, 455, and 473 nm deriving from $Dy^{3+} {}^6H_{15/2} \rightarrow {}^6P_{7/2}, {}^6P_{5/2}, {}^6I_{13/2}, {}^6G_{11/2}, {}^6I_{15/2},$ and $^6I_{9/2}$ transitions (Figure S6b).[49,50] The curve of the decay lifespan for **2** can be fitted by the double-exponential function, eq 2

$$[I = A_1 \exp(-t/\tau_1) + A_2 \exp(-t/\tau_2)] \tag{2}$$

and the mean lifespan is indexed through the function (eq 3)

$$[\tau^* = (A_1\tau_1^2 + A_2\tau_2^2)/(A_1\tau_1 + A_2\tau_2)] \tag{3}$$

The fitting results illustrate that $\tau_1, \tau_2,$ and τ^* for the 575 nm emission peak of **2** are 2.69, 10.76, and 7.44 μs, respectively, where τ_1 and τ_2 are, respectively, attributed to emission contributions of AMT moieties and Dy^{3+} centers (Figure 3d, Table S3).[51] Upon the 454 nm excitation, the emission spectrum of **3** (530–700 nm) shows a weak Ho^{3+} f–f emission band at 548 nm ($^5F_4 + {}^5S_2 \rightarrow {}^5I_8$) and a strong Ho^{3+} emission line at 660 nm ($^5F_5 \rightarrow {}^5I_8$) (Figure S6c). The excitation spectrum of **3** (250–480 nm) taken through supervising the dominant emission line at 660 nm reveals the OWCT of AMT fragments at 266 nm ($^1A_{1g} \rightarrow {}^1T_{1u}$) and two Ho^{3+} f–f excitation bands at 420 and 454 nm, respectively, stemming from $^5I_8 \rightarrow {}^5G_5$ and $^5I_8 \rightarrow {}^5G_6$ transitions (Figure 3e).[52,53] In line with the eqs 2 and 3, $\tau_1, \tau_2,$ and τ^* of the emission peak at 660 nm for **3** are 1.28, 10.64, and 5.54 μs, respectively, in which τ_1 and τ_2 can be responsible for the luminescence behaviors of AMT moieties and Ho^{3+} centers (Figure 3f, Table S3). On the basis of the 458 nm excitation, the emission spectrum of **4** (510–580 nm) displays two Er^{3+} f–f emission bands at 540 ($^2H_{11/2} \rightarrow {}^4I_{15/2}$) and 560 nm ($^2S_{3/2} \rightarrow {}^4I_{15/2}$) (Figure 3g). The excitation spectrum of **4** (240–475 nm) generates a strong OWCT of AMT moieties at 246 nm and two Er^{3+} f–f excitation bands at 416 and 458 ($^4I_{15/2} \rightarrow {}^4H_{9/2}$ and $^4F_{5/2}$) nm when the emission band is monitored at 540 nm (Figure S6d).[54] On the basis of eqs 2 and 3, $\tau_1, \tau_2,$ and τ^* of the emission band at 540 nm for **4** are suggested to be 1.30, 10.47, and 5.58 μs, respectively, in which τ_1 and τ_2 originate from emission behaviors of AMT moieties and Er^{3+} centers (Figure 3h, Table S3). In addition, for **2–4**, the broad backgrounds in their emission spectra may originate from the emission bands of $[B\text{-}\alpha\text{-}SbW_9O_{33}]^{9-}$ fragments in the structures. To prove the existence of the broad emission
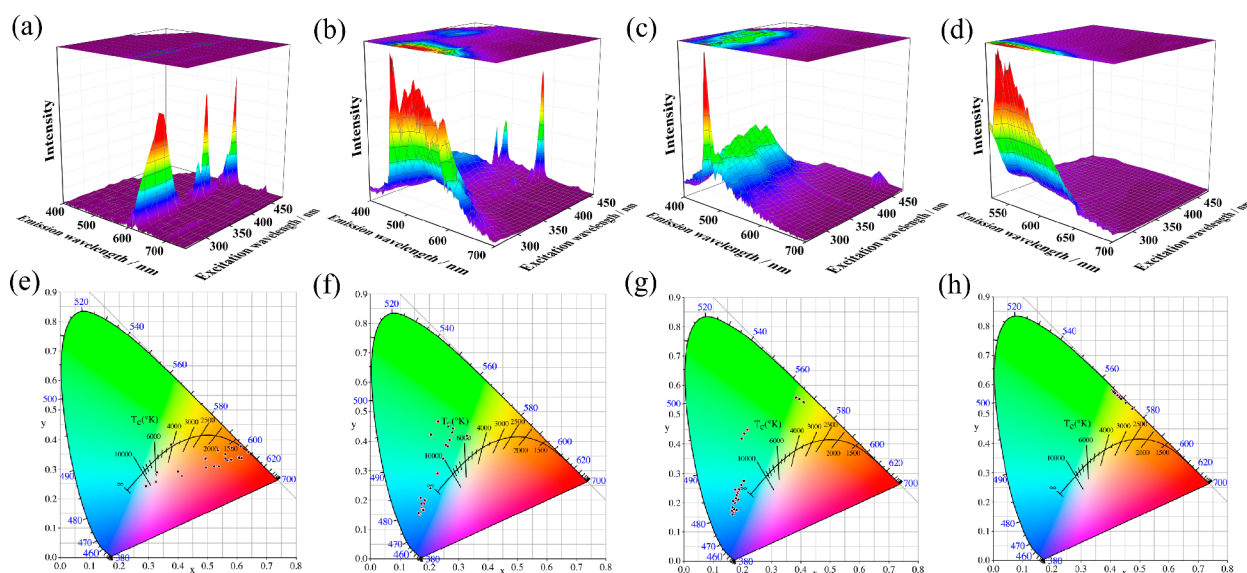
Figure 4. EEMs of (a) **1** (λ_{ex} = 250−470 nm), (b) **2** (λ_{ex} = 250−450 nm), (c) **3** (λ_{ex} = 250−470 nm), and (d) **4** (λ_{ex} = 250−470 nm). (e−h) CIE 1931 diagrams of **1**−**4**.

bands of [B-α-SbW$_9$O$_{33}$]$^{9-}$ fragments, we have measured the emission spectrum of solid-state Na$_9$[B-α-SbW$_9$O$_{33}$]·19.5H$_{22}$O under the excitation at 260 nm, which generates a broad emission band in the range of 400−600 nm (Figure S7a). We have also measured the emission spectra of Na$_9$[B-α-SbW$_9$O$_{33}$]·19.5H$_{22}$O under the excitation at 455, 454, and 458 nm (Figure S7b−d), which demonstrates that the backgrounds in the emission spectra of **2**−**4** measured under the excitation at 455, 454, and 458 nm all come from the [B-α-SbW$_9$O$_{33}$]$^{9-}$ fragments in the hosts. In line with our previous works, it can be found that there is a broad emission band (^{3}T$_{1u}$ → ^{1}A$_{1g}$) of [B-α-SbW$_9$O$_{33}$]$^{9-}$ fragments in the range of 400−600 nm.[25,33] According to the previous report of Yamase, there is a broad emission band (^{3}T$_{1u}$ → ^{1}A$_{1g}$) in the range of 400−600 nm of [SbW$_6$O$_{24}$]$^{7-}$ fragments.[47] Additionally, for **1**, there is no obvious emission band (^{3}T$_{1u}$ → ^{1}A$_{1g}$) of [B-α-SbW$_9$O$_{33}$]$^{9-}$ fragments in the emission spectrum of **1** in the range of 500−580 nm (Figure S8a,b) because the strong emission intensity of Eu^{3+} ions makes the emission intensity of [B-α-SbW$_9$O$_{33}$]$^{9-}$ fragments be negligible in the emission spectrum of **1**, and the ET from [B-α-SbW$_9$O$_{33}$]$^{9-}$ fragments to Eu^{3+} ions can also cause the emission intensity of [B-α-SbW$_9$O$_{33}$]$^{9-}$ fragments to become very faint in the emission spectrum of **1**. In contrast, the weak emission intensity of Dy^{3+}, Ho^{3+}, and Er^{3+} ions and the weak ET interactions from [B-α-SbW$_9$O$_{33}$]$^{9-}$ subunits to Dy^{3+}, Ho^{3+}, and Er^{3+} ions in **2**−**4** can result in the appearance of broad backgrounds from the emission bands of [B-α-SbW$_9$O$_{33}$]$^{9-}$ fragments in their emission spectra. Therefore, the broad backgrounds in the emission spectra of **2**−**4** come from the emission bands of [B-α-SbW$_9$O$_{33}$]$^{9-}$ subunits rather than the instrument system. Therefore, the emission in the spectra of **2**−**4** is assigned to the common contribution of the Ln^{3+} (Dy^{3+}, Ho^{3+}, Er^{3+}) centers and AMT moieties. We have measured the decay lifetime profiles of Na$_9$[B-α-SbW$_9$O$_{33}$]·19.5H$_{22}$O under excitation at 455, 454, and 458 nm. It can be found that τ_1, τ_2, and τ^* of the emission peak at 500 nm (λ_{ex} = 455 nm) are, respectively, 0.87, 6.52, and 3.24 μs (Figure S9a); τ_1, τ_2, and τ^* of the emission peak at 534 nm (λ_{ex} = 454 nm) are, respectively, 0.95, 6.84, and 3.49 μs (Figure S9b); and τ_1, τ_2, and τ^* of the emission

peak at 512 nm (λ_{ex} = 458 nm) are, respectively, 1.02, 6.10, and 3.16 μs (Figure S9c). Comparing the lifetime values of Na$_9$[B-α-SbW$_9$O$_{33}$]·19.5H$_{22}$O under excitation at 455, 454, and 458 nm with those of **2**−**4**, it can be concluded that the lifetimes τ_1 of **2**−**4** mainly come from the contribution of AMT moieties (Table S3).

The CIE 1931 diagram is convenient to help us acquire the authenticity of colors. Four primary optical parameters, such as the chromaticity coordinates (CCs), color purity (CP), dominant wavelength (DW), correlated color temperature (CCT), and quantum yield (QY), are usually collected by us. CCs can be employed to determine the actual emitted color for an emitter. The CP can be on behalf of the brightness of colors, which can comply with eq 4

$$CP = [(x - x_i)^2 + (y - y_i)^2 / (x_d - x_i)^2 + (y_d - y_i)^2]^{1/2} \tag{4}$$

in which (x, y), (x_i, y_i), and (x_d, y_d) represent the CCs for a light source, the CCs for white light (0.3333, 0.3333), and the DW for a luminescent material, respectively. The DW is related to the color combination of the emission spectrum and a light source. The feeling of an emitted light with a low CCT (<3000 K) is warm, that of a CCT of 3000−5000 K is comfortable, and that of a high CCT (>5000 K) is cool.[55−59]

The excitation wavelength regulation strategy is feasible to accomplish the emission color tuning of luminescent materials because different emission centers will selectively absorb special excited lights. Upon varying excitation wavelengths in the range of 250−470 nm for **1**, **3**, and **4** and 250−450 nm for **2**, corresponding CCs obtained from emission−excitation maps vary from (0.400, 0.291) to (0.639, 0.357), from (0.258, 0.386) to (0.328, 0.418), from (0.186, 0.211) to (0.409, 0.542), and from (0.428, 0.563) to (0.475, 0.517) for **1**−**4** (Figure 4a−h), which suggests that on the basis of the variation of excitation wavelengths, it is accessible to tune emitted colors from blue to red, blue to green, blue to yellow, and green to yellow for **1**−**4**. Relevant data of CCs, DWs, CPs, and CCTs for **1**−**4** are listed in Tables S4−S7. It is noteworthy that most of the CPs obtained at different excitations for **4** are >90% (Tables S7). The measured quantum yields (QYs) of **1**−
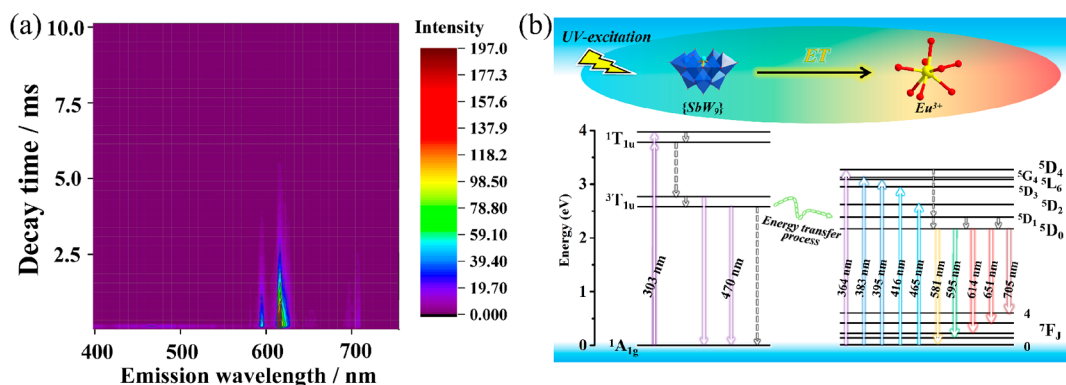
Figure 5. (a) TRES of **1** (λ_{ex} = 303 nm). (b) ET mechanism from AMT moieties to Eu^{3+} centers (broken lines: nonradiative transitions; full lines: radiative transitions).

4 are 8.05, 1.16, 1.99, and 0.04%, (Figure S10), which indicates that their quantum efficiencies are very low.

The appearance of the OWCT of AMT moieties in the excitation spectra of **1−4** manifests in that AMT moieties can transfer energy to Ln^{3+} ions under the OWCT excitation. Thus the TRES of **1−4** were carried out under their OWCT excitations to explore the ET process by analyzing the emission decay rate of different emission centers. As depicted in Figure 5a, the TRES of **1** generate a weak emission band of AMT moieties centered at 470 nm (ca. 400−500 nm) stemming from the $^3T_{1u} \rightarrow ^1A_{1g}$ triplet excitation transition and a series of Eu^{3+} f−f emission peaks at 581, 594, 614, 653, and 706 nm, which are ascribed to the $^5D_0 \rightarrow ^7F_K$ (K = 0, 1, 2, 3, 4) transitions, respectively. It can be observed from Figure 5a that the emission intensities of the $^3T_{1u} \rightarrow ^1A_{1g}$ transition of AMT moieties as well as the five characteristic emission peaks of Eu^{3+} centers reach the maximum at 100.0 μs and then decline to disappearance at 300.0 and 5400.0 μs, respectively, which manifests that the emission decay rate of Eu^{3+} centers is much slower than that of AMT moieties. It can be understood that the ET from AMT moieties to Eu^{3+} centers can dramatically inhibit the emission decay of Eu^{3+} centers. By virtue of the ET from AMT moieties to Eu^{3+} ions, the schematic ET process in **1** is depicted in Figure 5b. Upon the OWCT excitation at 303 nm, electrons in the $^1A_{1g}$ ground state of AMT moieties jump to the high excited state ($^1T_{1u}$) and then quickly relax to the lower $^3T_{1u}$ state by a nonradiative transition. Part of the energy in the $^3T_{1u}$ state promotes the $^3T_{1u} \rightarrow ^1A_{1g}$ emission transition; in the meantime, part of the energy in the $^3T_{1u}$ state of the AMT moieties transfers to the $^5D_1$ state of the Eu^{3+} centers, relying on the overlap between the $^3T_{1u}$ state (2.64 eV) of the AMT moieties and the $^5D_1$ state (2.32 eV) of the Eu^{3+} centers, and then relaxes to the $^5D_0$ state (2.14 eV), leading to the $^5D_0 \rightarrow ^7F_K$ (K = 0, 1, 2, 3, 4) emission of Eu^{3+} centers (Table S8). The ET process is mainly completed in the form of energy reabsorption; that is, Eu^{3+} centers (acceptors) reabsorb the emitted light of the AMT moieties (donors), which can be responsible for the ET process. As seen from the TRES of **2−4**, the emission decay rate cannot be effectively inhibited by the ET from AMT moieties to Dy^{3+}, Ho^{3+}, and Er^{3+} centers (Figure S11a−c); therefore, the ET processes in **2−4** have not been discussed in this Article.

CONCLUSIONS

In total, we have triumphantly prepared a series of OLALnAMTs **1−4** through adopting a two-template-agent strategy. The capped {HPO_3} and {WO_4} tetrahedral groups simultaneously perform as structure-directing templates to induce the assembly of **1−4**. In terms of the synthesis challenge of novel OLALnAMT materials, the double-template-agent method can be regarded as an efficient pathway to control the architectures of POAs. Upon UV excitation, **1−4** show their unique luminescence behaviors. On the basis of the modulation of the excitation wavelength, their emission colors could be regulated from blue to red, blue to green, blue to yellow, and green to yellow for **1−4**. The ET analysis in **1** indicates that AMT moieties can prolong the emission decay rate of Eu^{3+} centers through the ET from the OWCT emission of AMT moieties to the characteristic emission transitions of Eu^{3+} centers. The measurements and investigations of the luminescence performances of **1−4** may confirm the great potential of OLALnAMTs in optic applications.

■ ASSOCIATED CONTENT

ⓢ Supporting Information

The Supporting Information is available free of charge at https://pubs.acs.org/doi/10.1021/acs.inorgchem.0c03148.

> Relevant architecture diagrams, infrared spectra and thermogravimetric profiles, and related luminescence spectra and TRES (PDF)

Accession Codes

CCDC 2020540−2020543 for **1−4** includes the supplementary crystallographic data for this paper. These data can be acquired free of charge via www.ccdc.cam.ac.uk/data_request/cif, or by emailing data_request@ccdc.cam.ac.uk, or by contacting The Cambridge Crystallographic Data Centre, 12, Union Road, Cambridge CB2 1EZ, UK; fax: + 44 1223 336033.

■ AUTHOR INFORMATION

Corresponding Authors

Lijuan Chen − *Henan Key Laboratory of Polyoxometalate Chemistry, College of Chemistry and Chemical Engineering, Henan University, Kaifeng, Henan 475004, China;* Email: ljchen@henu.edu.cn

Junwei Zhao − *Henan Key Laboratory of Polyoxometalate Chemistry, College of Chemistry and Chemical Engineering, Henan University, Kaifeng, Henan 475004, China;* ⓞ orcid.org/0000-0002-7685-1309; Email: zhaojunwei@henu.edu.cn

Authors

Xin Xu − Henan Key Laboratory of Polyoxometalate Chemistry, College of Chemistry and Chemical Engineering, Henan University, Kaifeng, Henan 475004, China

Xiaoyi Liu − Henan Key Laboratory of Polyoxometalate Chemistry, College of Chemistry and Chemical Engineering, Henan University, Kaifeng, Henan 475004, China

Dan Wang − Henan Key Laboratory of Polyoxometalate Chemistry, College of Chemistry and Chemical Engineering, Henan University, Kaifeng, Henan 475004, China

Xuejun Liu − Henan Key Laboratory of Polyoxometalate Chemistry, College of Chemistry and Chemical Engineering, Henan University, Kaifeng, Henan 475004, China

Complete contact information is available at:
https://pubs.acs.org/10.1021/acs.inorgchem.0c03148

Notes

The authors declare no competing financial interest.

■ REFERENCES

(1) Zhang, Z. M.; Duan, X.; Yao, S.; Wang, Z.; Lin, Z.; Li, Y. G.; Long, L. S.; Wang, E. B.; Lin, W. B. Cation-mediated optical resolution and anticancer activity of chiral polyoxometalates built from entirely achiral building blocks. *Chem. Sci.* **2016**, *7*, 4220−4229.

(2) Jin, L.; Zhu, Z. K.; Wu, Y. L.; Qi, Y. J.; Li, X. X.; Zheng, S. T. Record high-nuclearity polyoxoniobates: discrete nanoclusters {Nb₁₁₄}, {Nb₈₁}, and {Nb₅₂}, and extended frameworks based on {Cu₃Nb₇₈} and {Cu₄Nb₇₈}. *Angew. Chem., Int. Ed.* **2017**, *56*, 16288−16292.

(3) Zheng, Q.; Vila-Nadal, L.; Lang, Z.; Chen, J.-J.; Long, D.-L.; Mathieson, J. S.; Poblet, J. M.; Cronin, L. Self-sorting of heteroanions in the assembly of cross-shaped polyoxometalate clusters. *J. Am. Chem. Soc.* **2018**, *140*, 2595−2601.

(4) Symes, M. D.; Kitson, P. J.; Yan, J.; Richmond, C. J.; Cooper, G. J. T.; Bowman, R. W.; Vilbrandt, T.; Cronin, L. Integrated 3D-printed reaction ware for chemical synthesis and analysis. *Nat. Chem.* **2012**, *4*, 349−354.

(5) Yang, K.; Hu, Y. Y.; Li, L. Y.; Cui, L. L.; He, L.; Wang, S. J.; Zhao, J. W.; Song, Y. F. First high-nuclearity mixed-valence polyoxometalate with hierarchical interconnected Zn²⁺ migration channels as an advanced cathode material in aqueous zinc-ion battery. *Nano Energy* **2020**, *74*, 104851.

(6) Wang, Y.; Wu, Z. K.; Yu, H.; Han, S.; Wei, Y. G. Highly efficient oxidation of alcohols to carboxylic acids using a polyoxometalate-supported chromium(III) catalyst and CO₂. *Green Chem.* **2020**, *22*, 3150−3154.

(7) Yang, Y.; Jia, T.; Han, Y. Z.; Nan, Z. A.; Yuan, S. F.; Yang, F. L.; Sun, D. An all-alkynyl protected 74-nuclei silver(I)−copper(I)-oxo nanocluster: oxo-induced hierarchical bimetal aggregation and anisotropic surface ligand orientation. *Angew. Chem.* **2019**, *131*, 12408−12413.

(8) Bannani, F.; Floquet, S.; Leclerc-Laronze, N.; Haouas, M.; Taulelle, F.; Marrot, J.; Kögerler, P.; Cadot, E. Cubic box versus spheroidal capsule built from defect and intact pentagonal units. *J. Am. Chem. Soc.* **2012**, *134*, 19342−19345.

(9) Bassil, B. S.; Ibrahim, M.; Al-Oweini, R.; Asano, M.; Wang, Z.; van Tol, J.; Dalal, N. S.; Choi, K. Y.; Ngo Biboum, R.; Keita, B.; Nadjo, L.; Kortz, U. A planar {Mn₁₉(OH)₁₂}²⁶⁺ unit incorporated in a 60-tungsto-6-silicate polyanion. *Angew. Chem., Int. Ed.* **2011**, *50*, 5961−5964.

(10) Zhan, C. H.; Zheng, Q.; Long, D. L.; Vilà-Nadal, L.; Cronin, L. Controlling the reactivity of the [P₈W₄₈O₁₈₄]⁴⁰⁻ inorganic ring and its assembly into POMZite inorganic frameworks with silver ions. *Angew. Chem.* **2019**, *131*, 17442−17446.

(11) Ma, P. T.; Hu, F.; Wang, J. P.; Niu, J. Y. Carboxylate covalently modified polyoxometalates: from synthesis, structural diversity to applications. *Coord. Chem. Rev.* **2019**, *378*, 281−309.

(12) Miras, H. N.; Yan, J.; Long, D. L.; Cronin, L. Engineering polyoxometalates with emergent properties. *Chem. Soc. Rev.* **2012**, *41*, 7403−7430.

(13) Liu, H.; Qin, C.; Wei, Y. G.; Xu, L.; Gao, G. G.; Li, F. Y.; Qu, X.-S. Copper-complex-linked polytungsto-bismuthate (-antimonite) chain containing sandwich Cu(II) ions partially modified with imidazole ligand. *Inorg. Chem.* **2008**, *47*, 4166−4172.

(14) Raula, M.; Gan Or, G.; Saganovich, M.; Zeiri, O.; Wang, Y.; Chierotti, M. R.; Gobetto, R.; Weinstock, I. A. Polyoxometalate complexes of anatase-titanium dioxide cores in water. *Angew. Chem., Int. Ed.* **2015**, *54*, 12416−12421.

(15) Ritchie, C.; Moore, E. G.; Speldrich, M.; Kögerler, P.; Boskovic, C. Terbium polyoxometalate organic complexes: correlation of structure with luminescence properties. *Angew. Chem., Int. Ed.* **2010**, *49*, 7702−7871.

(16) Shang, S. X.; Lin, Z. G.; Yin, A. X.; Yang, S.; Chi, Y. N.; Wang, Y.; Dong, J.; Liu, B.; Zhen, N.; Hill, C. L.; Hu, C. Self-assembly of Ln(III)-containing tungstotellurates(VI): correlation of structure and photoluminescence. *Inorg. Chem.* **2018**, *57*, 8831−8840.

(17) Chen, W. C.; Jiao, C. Q.; Wang, X. L.; Shao, K. Z.; Su, Z. M. Self-assembly of nanoscale lanthanoid-containing selenotungstates: synthesis, structures, and magnetic studies. *Inorg. Chem.* **2019**, *58*, 12895−12904.

(18) Song, Y.-F.; Cronin, L. Postsynthetic covalent modification of metal−organic framework (MOF) materials. *Angew. Chem., Int. Ed.* **2008**, *47*, 4635−4637.

(19) Nohra, B.; Mialane, P.; Dolbecq, A.; Rivière, E.; Marrot, J.; Sécheresse, F. Heterometallic 3d−4f cubane clusters inserted in polyoxometalate matrices. *Chem. Commun.* **2009**, *40*, 2703−2705.

(20) An, H.; Han, Z.; Xu, T. Three-dimensional architectures based on lanthanide-substituted double-Keggin-type polyoxometalates and lanthanide cations or lanthanide-organic complexes. *Inorg. Chem.* **2010**, *49*, 11403−11414.

(21) Li, L. L.; Han, H. Y.; Wang, Y. H.; Tan, H. Q.; Zang, H. Y.; Li, Y. G. Construction of polyoxometalates from dynamic lacunary polyoxotungstate building blocks and lanthanide linkers. *Dalton Trans.* **2015**, *44*, 11429−11436.

(22) Chen, L. J.; Cao, J.; Li, X.; Ma, X.; Luo, J.; Zhao, J. W. The first purely inorganic polyoxotungstates constructed from dimeric tungstoantimonate-based iron−rare-earth heterometallic fragments. *CrystEngComm* **2015**, *17*, 5002−5013.

(23) Artetxe, B.; Reinoso, S.; San Felices, L.; Lezama, L.; Gutierrez-Zorrilla, J. M.; Vicent, C.; Haso, F.; Liu, T. New perspectives for old clusters: Anderson−Evans anions as building blocks of large polyoxometalate frameworks in a series of heterometallic 3d−4 f species. *Chem. - Eur. J.* **2016**, *22*, 4616−4625.

(24) Chen, Y. H.; Sun, L. H.; Chang, S. Z.; Chen, L. J.; Zhao, J. W. Synergistic effect between different coordinate geometry of lanthanide and various coordination mode of 2-picolinic acid ligand tuning three types of rare 3d−4f heterometallic tungstoantimonates. *Inorg. Chem.* **2018**, *57*, 15079−15092.

(25) Xu, X.; Chen, Y. H.; Zhang, Y.; Liu, Y. F.; Chen, L. J.; Zhao, J. W. Rare-earth and antimony-oxo clusters simultaneously connecting antimonotungstates comprising divacant and tetravacant Keggin fragments. *Inorg. Chem.* **2019**, *58*, 11636−11648.

(26) Gao, J.; Yan, J.; Beeg, S.; Long, D. L.; Cronin, L. One-pot versus sequential reactions in the self-assembly of gigantic nanoscale polyoxotungstates. *J. Am. Chem. Soc.* **2013**, *135*, 1796−1805.

(27) Liu, J. C.; Han, Q.; Chen, L. J.; Zhao, J. W.; Streb, C.; Song, Y. F. Aggregation of giant cerium−bismuth tungstate clusters into a 3D

porous framework with high proton conductivity. *Angew. Chem., Int. Ed.* **2018**, *57*, 8416−8420.

(28) Wu, H.; Yan, B.; Liang, R.; Singh, V.; Ma, P.; Wang, J.; Niu, J. Y. An organic chromophore-modified samarium-containing polyoxometalate: excitation-dependent color tunable behavior from the organic chromophores to the lanthanide ion. *Dalton Trans.* **2020**, *49*, 388−394.

(29) Gao, J.; Yan, J.; Mitchell, S. G.; Miras, H. N.; Boulay, A. G.; Long, D.-L.; Cronin, L. Self-assembly of a family of macrocyclic polyoxotungstates with emergent material properties. *Chem. Sci.* **2011**, *2*, 1502−1508.

(30) Yaghi, O. M.; O'Keeffe, M.; Ockwig, N. W.; Chae, H. K.; Eddaoudi, M.; Kim, J. Reticular synthesis and the design of new materials. *Nature* **2003**, *423*, 705−714.

(31) Cheetham, A. K.; Rao, C. N. R. There's room in the middle. *Science* **2007**, *318*, 58−59.

(32) Li, X. X.; Fang, W. H.; Zhao, J. W.; Yang, G. Y. The first 3-connected SrSi$_2$-type 3D chiral framework constructed from {Ni$_6$PW$_9$} building units. *Chem. - Eur. J.* **2015**, *21*, 2315−2318.

(33) Xu, X.; Meng, R. R.; Lu, C. T.; Mei, L.; Chen, L. J.; Zhao, J. W. Acetate-decorated tri-Ln(III)-containing antimonotungstates with a tetrahedral {WO$_4$} group as a structure-directing template and their luminescence properties. *Inorg. Chem.* **2020**, *59*, 3954−3963.

(34) Marrot, J.; Pilette, M. A.; Haouas, M.; Floquet, S.; Taulelle, F.; López, X.; Poblet, J. M.; Cadot, E. Assembly and autochirogenesis of a chiral inorganic polythioanion mobius strip via symmetry breaking. *J. Am. Chem. Soc.* **2012**, *134*, 1724−1737.

(35) Ibrahim, M.; Mal, S. S.; Bassil, B. S.; Banerjee, A.; Kortz, U. yttrium(III)-containing tungstoantimonate(III) stabilized by tetrahedral WO$_4^{2-}$ capping unit, [{Y(r-SbW$_9$O$_{31}$(OH)$_2$)(CH$_3$COO)-(H$_2$O)}$_3$(WO$_4$)]$^{17-}$. *Inorg. Chem.* **2011**, *50*, 956−960.

(36) Cai, J.; Zheng, X. Y.; Xie, J.; Yan, Z. H.; Kong, X. J.; Ren, Y. P.; Long, L.-S.; Zheng, L.-S. Anion-dependent assembly of heterometallic 3d−4f clusters based on a lacunary polyoxometalate. *Inorg. Chem.* **2017**, *56*, 8439−8445.

(37) Liang, Z.; Li, L.; Zhang, Y.; Ma, P.; Niu, J.; Wang, J. Two novel heteropolyniobates using TeO$_3^{2−}$ as template and linker. *Inorg. Chem.* **2019**, *58*, 27−30.

(38) Almeida Paz, F. A.; Klinowski, J.; Vilela, S. M. F.; Tome, J. P. C.; Cavaleiro, J. A. S.; Rocha, J. Ligand design for functional metal−organic frameworks. *Chem. Soc. Rev.* **2012**, *41*, 1088−1110.

(39) Eliseeva, S. V.; Bunzli, J. C. G. Lanthanide luminescence for functional materials and bio-sciences. *Chem. Soc. Rev.* **2010**, *39*, 189−227.

(40) Zhao, J. W.; Li, Y. Z.; Chen, L. J.; Yang, G. Y. Research progress on polyoxometalate-based transition-metal−rare-earth heterometallic derived materials: synthetic strategies, structural overview and functional applications. *Chem. Commun.* **2016**, *52*, 4418−4445.

(41) Armelao, L.; Quici, S.; Barigelletti, F.; Accorsi, G.; Bottaro, G.; Cavazzini, M.; Tondello, E. Design of luminescent lanthanide complexes: From molecules to highly efficient photo-emitting materials. *Coord. Chem. Rev.* **2010**, *254*, 487−505.

(42) Banerjee, A. K.; Mukhopadhyay, A. K.; Mukherjee, R. K.; Chowdhury, M. $^7F_0$-$^5D_1$ transition in Eu^{3+}—hexakisantipyrene-triiodide single crystal. a magnetic dipole transition. *Chem. Phys. Lett.* **1979**, *67*, 418−419.

(43) Li, H.; Zhao, R.; Jia, Y.; Sun, W.; Fu, J.; Jiang, L.; Zhang, S.; Pang, R.; Li, C. Sr$_{1.7}$Zn$_{0.3}$CeO$_4$: Eu^{3+} novel red-emitting phosphors: synthesis and photoluminescence properties. *ACS Appl. Mater. Interfaces* **2014**, *6*, 3163−3169.

(44) Wang, J. W.; Chang, Y. M.; Chang, H. C.; Lin, S. H.; Huang, L. C. L.; Kong, X. L.; Kang, M.-W. Local structure dependence of the charge transfer band in nanocrystalline Y$_2$O$_3$: Eu^{3+}. *Chem. Phys. Lett.* **2005**, *405*, 314−317.

(45) Wei, Z.; Sun, L.; Liao, C.; Yin, J.; Jiang, X.; Yan, C.; Lü, S. Size-dependent chromaticity in YBO$_3$:Eu nanocrystals: correlation with microstructure and site symmetry. *J. Phys. Chem. B* **2002**, *106*, 10610−10617.

(46) Carrasco, I.; Piccinelli, F.; Romet, I.; Nagirnyi, V.; Bettinelli, M. Competition between energy transfer and energy migration processes in neat and Eu^{3+}-Doped TbPO$_4$. *J. Phys. Chem. C* **2018**, *122*, 6858−6864.

(47) Yamase, T. Photo- and electrochromism of polyoxometalates and related materials. *Chem. Rev.* **1998**, *98*, 307−325.

(48) Zmojda, J.; Kochanowicz, M.; Miluski, P.; Dorosz, J.; Pisarska, J.; Pisarski, W. A.; Dorosz, D. Investigation of upconversion luminescence in antimony−germanate double-clad two cores optical fiber co-doped with Yb^{3+}/Tm^{3+} and Yb^{3+}/Ho^{3+} ions. *J. Lumin.* **2016**, *170*, 795−800.

(49) Zhang, Y.; Gong, W.; Yu, J.; Pang, H.; Song, Q.; Ning, G. A new single-phase white-light-emitting CaWO$_4$:Dy^{3+} phosphor: synthesis, luminescence and energy transfer. *RSC Adv.* **2015**, *5*, 62527−62533.

(50) Fu, Z. L.; Xia, W. W.; Li, Q. S.; Cui, X. Y.; Li, W. H. Highly uniform NaLa(MoO$_4$)$_2$:Ln^{3+} (Ln = Eu, Dy) microspheres: template-free hydrothermal synthesis, growing mechanism, and luminescent properties. *CrystEngComm* **2012**, *14*, 4618−4624.

(51) Zhou, J.; Xia, Z. G. Luminescence color tuning of Ce^{3+}, Tb^{3+} and Eu^{3+} codoped and tri-doped BaY$_2$Si$_3$O$_{10}$ phosphors via energy transfer. *J. Mater. Chem. C* **2015**, *3*, 7552−7560.

(52) Wei, Z.; Sun, L.; Liao, C.; Yin, J.; Jiang, X.; Yan, C.; Lu, S. Z. Size-dependent chromaticity in YBO$_3$:Eu nanocrystals: correlation with microstructure and site symmetry. *J. Phys. Chem. B* **2002**, *106*, 10610−10617.

(53) Yu, Y.; Zheng, Y.; Qin, F.; Liu, L.; Zheng, C.; Chen, G.; Zhang, Z.; Cao, W. Influence of Yb^{3+} concentration on upconversion luminescence of Ho^{3+}. *Opt. Commun.* **2011**, *284*, 1053−1056.

(54) Yan, L.; Zhou, B.; Song, N.; Liu, X.; Huang, J.; Wang, T.; Tao, L.; Zhang, Q. Self-sensitization induced upconversion of Er^{3+} in core−shell nanoparticles. *Nanoscale* **2018**, *10*, 17949−17957.

(55) Wang, Q.; Xu, H. S.; Zhang, F. Z.; Wang, Z. H. Influence of color temperature on comfort and preference for LED indoor lighting. *Optik* **2017**, *129*, 21−29.

(56) Kapogiannatou, A.; Paronis, E.; Paschidis, K.; Polissidis, A.; Kostomitsopoulos, N. G. Effect of light colour temperature and intensity on $τhε$ behaviour of male C57CL/6J mice. *Appl. Anim. Behav. Sci.* **2016**, *184*, 135−140.

(57) Zhang, Y.; Gong, W.; Yu, J.; Lin, Y.; Ning, G. Tunable white-light emission via energy transfer in single-phase LiGd (WO$_4$)$_2$: Re^{3+} (Re= Tm, Tb, Dy, Eu) phosphors for UV-excited WLEDs. *RSC Adv.* **2015**, *5*, 96272−96280.

(58) Suresh Kumar, J.; Pavani, K.; Mohan Babu, A.; Kumar Giri, N.; Rai, S. B.; Moorthy, L. R. Fluorescence characteristics of Dy^{3+} ions in calcium fluoroborate glasses. *J. Lumin.* **2010**, *130*, 1916−1923.

(59) McCamy, C. S. Correlated color temperature as an explicit function of chromaticity coordinates. *Color Res. Appl.* **1992**, *17*, 142−144.